Supplemental Material

Journal of Physical Oceanography
Why Does the Deep Western Boundary Current "Leak" Around Flemish Cap?
https://doi.org/10.1175/JPO-D-19-0247.1

Why does the Deep Western Boundary Current "leak" around Flemish Cap? Supplementary Material

Aviv Solodoch[*], James C. McWilliams[*], Andrew L. Stewart[*], Jonathan Gula[**], and Lionel Renault[†]

[*]Dept. of Atmoshperic and Oceanic Sciences, UCLA, Los Angeles, California
[**]Univ. Brest, CNRS, IRD, Ifremer, LOPS, IUEM, Brest, France
[†]LEGOS, University of Toulouse, IRD, CNRS, CNES, UPS, Toulouse, France

All sections referenced here are in regards to the main manuscript rather than supplementary material sections.

1 Tracer diffusion noise

For the GB_B ROMS solution (section 2a), split-rotated third-order upwind (RSUP3) tracer advection is used [1]. We initially used the RSUP3 version in which the diffusive component is rotated to align with isoneutral coordinates [2], but found that severe grid-scale noise appeared at depth (especially near the bottom), including in vertical velocity, and was accompanied by temperature drift in the same locations. The problem appears to be accentuated by high spatial resolution, and does not appear or is greatly diminished in CROCO implementations of resolution twice coarser or more in our experience, e.g., the parent domain [3] used for the GB_B boundary conditions (section 2a). It is likely related to simplifying approximations made in the estimation of isoneutral-direction derivatives in the CROCO version we use (personal communication from Florian Lemarié). To circumvent the problem, we reverted to the isopotential-rotated RSUP3 version [1], and reinitialized the model solution. The noise and severe temperature drift did not occur in the isopotential configuration. Water mass biases that do appear in the final configuration are typical of numerical models in the subpolar region (appendix B); these biases have lower amplitude and a different spatial structure than encountered in the isoneutral noise case.

2 Loss of ExPath floats around Flemish Cap

The number of ExPath floats that have left the DWBC around FC (section 3a) is estimated from reviewing individual trajectories and their time dependence (not shown). Despite some trajectory gaps (section 2a), it appears relatively clear that 33 of the 55 floats with usable trajectories (Sec. 2b) have left the DWBC around FC (see also [4], figure 2b). Here the 45 N latitude is used as the boundary between south FC and the GB. Changing the limit by up to almost 0.5 degree to the north and more to the south, does not change these numbers. Five additional floats have likely left the DWBC at either south FC or east GB, which remains uncertain since their trajectories are less complete in their loss region. Ten floats have crossed south through Flemish Pass rather than travel around FC (see also [5])[1]. Therefore $73-84\%$ of all floats that traveled around FC (i.e., excluding floats traveling through Flemish Cap), were lost ("leaked") from the DWBC to the interior before circumventing this topographic feature.

The distributions of points where floats have crossed the 4 km isobath offshore are shown separately for the 1500 and 700 m ballasted ExPath floats in supplementary figure 1a. Compare it with figure 3a in the paper, showing the combined 1500 and 700 m floats distribution. The 1500 m distribution appears qualitatively similar to the combined. The 700 m distribution and is neither distinctly similar or distinctly different from the 1500 m distribution. Since the former set includes only 12 floats, we do not attempt a quantitative comparison. The model particle diagnostics do allow a comparison between the different depths (supplemental subsection 4).

[1]Flemish Pass has a 1100 m deep sill, and all floats crossing it were of the 700 dbar ballast type.

3 Statistical significance of Lagrangian velocity average

Statistical significance of Lagrangian mean quantities (section 3a) in each grid cell was determined approximately by the condition that $|\overline{v_c}| > 2S(v_c)$. Here an overbar denotes the simple mean estimator, a sample average, while $S(\cdot)$ denotes an estimator of the error of the sample average. Two error estimators were tested. The first was $S_e = STD/\sqrt{N_e}$. Here STD stands for the standard deviation of all v_c measurements, N_e is the effective number of degrees of freedom. In our estimate for N_e we account for consecutive population of a grid cell by the same particle. We do not account for co-population of a grid cell by particles from different Orphan Knoll Line releases. This type of event is likely rare, since auto-correlation time in this area [6, 7], 5-10 days, is no longer than intervals between releases (10 days), and due to the fine grid resolution. The approximation $N_e = N/n$ was made separately for each grid cell, where N is the number of samples used to calculate $|\overline{v_c}|$, and $n = Adx/|\overline{v_c}dt|$ is the average number of TrajInt time samples (with time step dt) required for a particle to leave a grid cell (of length dx). The factor $A = 0.25$ approximately accounts for the two-dimensional geometry, assuming entry directions into cells are random. The second error estimator is based on the standard deviation (STD_{MA}) of annual v_c averages over $N_Y = 8$ years (model years 9-16) $S_M = STD_{MA}/\sqrt{N_Y}$. Both methods yielded similar results, and hence the second, simpler method is used to define statistically significant values in figure 3c.

4 Additional Lagrangian mean diagnostics for model particles

To complement paper figure 3, where the Lagrangian-mean quantities were shown for particles initialized over 1500 m depth, we display the same diagnostics for particles initialized over 700 m depth in supplementary figure 1 below. The results are very similar to 1500 m particles results. One difference is the transport of 700 m particles through Flemish Pass (the $\approx$ 1100 m deep channel west of Flemish Cap, FC in the figure). A second difference is that 700 m particles have statistically significant velocity further downstream than 1500 m initialized particles, including west of Grand Banks. For this reason, the displayed area in supplementary figure 1b is larger than in paper figure 3b.

5 EKE comparison with altimetry and degradation with resolution

The model surface geostrophic EKE (appendix B) is about five times larger than the altimetric estimates based on the DUACS L4 merged reprocessed product [8], in a region around FC (figure B1(c-d). Lower altimetric EKE is to be expected, since the model (GB_B) horizontal grid resolution is about 10 times higher than that of the altimetric product. In addition, the objective mapping technique applied in constructing the altimetric product is associated with coarser scales than its grid resolution. Indeed it is well documented that the altimetric product is biased low in EKE [8]. The unresolved scales contribute much of the difference in energy. For example, while the locations of elevated EKE are generally in agreement between the panels, the altimetric product shows no elevated values near the Labrador Current, which has width close to the product resolution. These issues are likely exacerbated since the Rossby radius of deformation in the region is close to or lower than the altimetric product resolution. Additionally, it is possible that model EKE is biased high due to not including current-atmosphere feedback parameterization [3, 9, 10].

To roughly gauge the effect of coarser resolution sampling on the model EKE, we applied a spatial Gaussian low pass filter (LPF) to GB_B SSH fields in calculation of (low-passed) EKE. Two different LPFs were tested separately. A 1/4 degree standard-deviation (std) LPF approximately represents a 25 km grid resolution. The 1/4 degree LPF applied to the model fields results in only a 40% EKE reduction within the same region. However, the effective spatial and temporal resolutions of the altimetric product are generally lower than its grid resolution and sample intervals, respectively. These depend on the details of the objective mapping method applied to the multiple-satellite data set (see appendix B in [8]). The enforced DUACS-L4 data correlation scales of observations to derived fields are $\geq 100km$ and ≥ 15 *days* at the latitudes considered in figure B1. In addition the observation covariance matrix is constructed on a 1 degree grid. Thus, to account for the objective mapping effective resolution in a rough approximation, we thus exchange the 1/4 degree LPF for a 100 km std LPF. According to [11], effective numerical model resolution is about 5 $\times$ the grid resolution. Therefore effective numerical (GB_B) model resolution is $\approx$ 12.5 km, and hence the 100 km std LPF is a reasonable method of comparison with the altimetric product. The resulting GB_B model spatially averaged LPF EKE (not shown) is within a few percent of the spatially-averaged altimetric observations within the region, demonstrating that the discrepancy in amplitude of the unfiltered model EKE compared with altimetry, is largely due to lower effective altimetric product resolution.

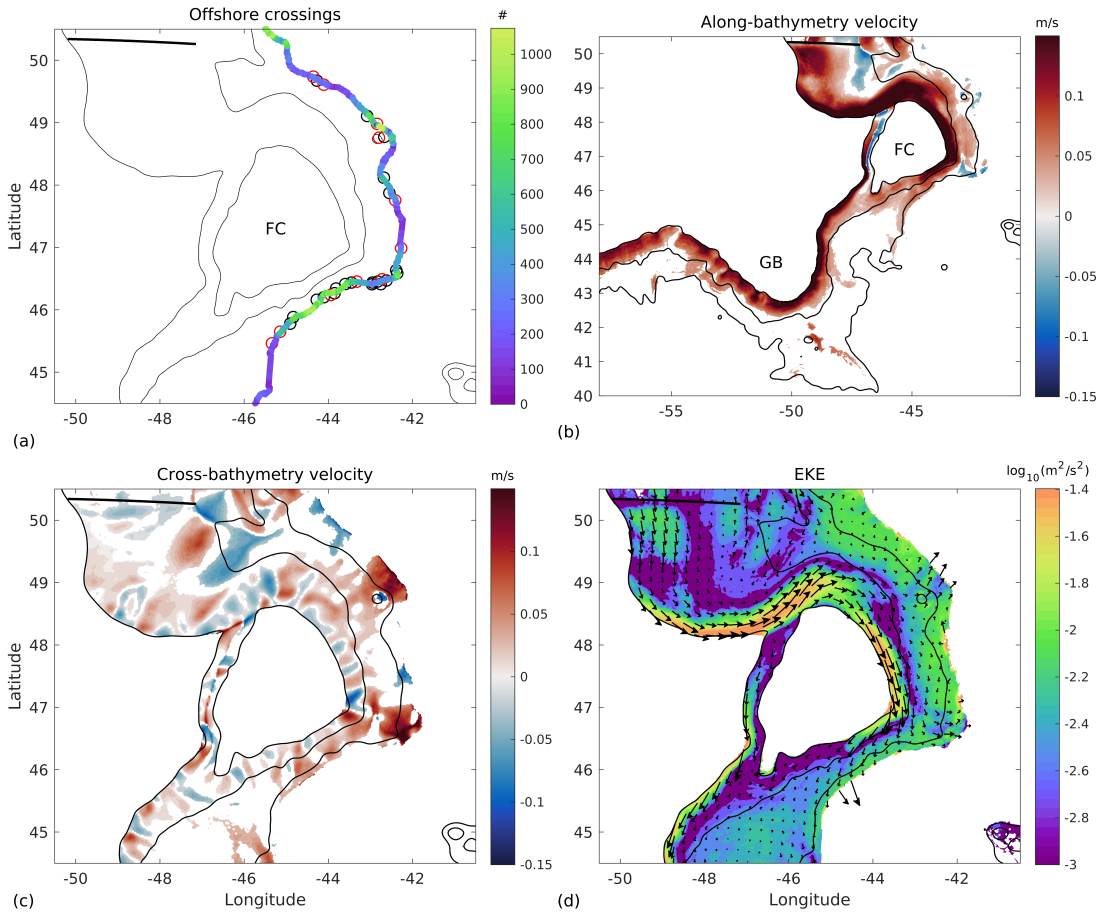

Figure 1: The figure is identical to figure 3 in the paper, except that model particles initialized at 700 m depth (rather than 1500 m) are used here, ExPath particles are color coded for depths in panel a, and a larger area is displayed in panel b. (a) Locations at which the ExPath floats (circles, red for 700 and blue for 1500 m depths) and 700 m depth-initialized Exp3d particles (colors) first cross the 4 km isobath. The colors correspond to the number of model particles crossing the 4 km isobath at each model gridpoint along the isobath. (b) Lagrangian-mean along-bathymetry velocity component (positive ≈ downstream), (c) Lagrangian-mean cross-bathymetry velocity component (positive offshore), and (d) Lagrangian eddy kinetic energy (EKE) derived from the Exp3d particles initialized at 1500 m depth (see section 3c for definitions). In panels b-c, only statistically significant values are displayed, i.e., white patches are not associated with significant values. Lagrangian mean velocity vectors are superimposed in panel d. The 1, 3, and 4 km isobaths are marked with black contours in each panel. The deployment line (OKL) of model particles is marked by the thick black line. The bathymetric features of Flemish Cap and the Grand Banks of Newfoundland are marked by the letters FC and GB, respectively, in panels a-b.

6 Statistical comparison of model and observed DWBC transports

The model mean DWBC transport at the 47 N section east of Flemish Cap (FC) , 58.5 ± 29.8 Sv, is considerably higher than the observational value [12], 30.7 ± 7.4 Sv, an average of six summer-time LADCP ship-sections, from different years. Additionally the observations were taken in summertime, and May-August model mean transport is even 5.5 Sv higher. Here we defined the Eulerian mean transport as the sum over all southward transport cells west of 41 W, of the time-mean Eulerian velocity section. Note that M14 used a different definition, obtaining 37.47 ± 7.4 Sv. The model transport standard deviation is based on transport estimates over all (2-day) output samples from years 9-16, a total of 1460 samples. The time samples may be taken as approximately independent, since on the continental slope, variability over time scale of a few days is high [12], likely due to topographic Rossby waves. A more conservative approach, where the number of effective degrees of freedom is halved (analogous to a 4-day integral scale) leads to only a 3rd significant digit change in the p value we quote below. Since six observations are likely not enough to estimate variability well, we make the assumption that the variance of the distributions from which the model and observed samples were taken are equal, leading to equation 5.9 for the test statistic z in [13],

$$z = \frac{\overline{x_1} - \overline{x_2}}{\sqrt{\frac{1}{n_1} + \frac{1}{n_2}} \sqrt{\frac{(n_1-1)s_1^2 + (n_2-1)s_2^2}{n_1+n_2-2}}}. \tag{1}$$

Here x_i is the transport mean, n_i is the number of degrees of freedom, and s_i is the standard deviation, within set i, i.e., the ROMS or observational [12] data. The test statistic value is then $z = 2.27$, leading to significance $p = 0.0231$ for a two-sided test. Therefore, the null hypothesis that the true means are equal is rejected. The high model transport is similar to the results of the VIKING20 numerical model employed by M14, 60.3 ± 23.6 Sv. However, in the next subsection we show that the model DWBC transport is in excellent agreement with observations in other locations, and suggest a reason for the reason for gross model disagreement with the M14 observations.

7 Additional model DWBC transport validation

Here we show evidence that within the GB_B simulation, the high DWBC transport relative to observations at the [12] (M14) section is partially the result of southward flow on the western flank of the southern cyclonic recirculation to the east of the DWBC (figure 4). The cyclonic recirculations around FC have been reported previously based on observations and other numerical models as well (section 3b). The GB_B DWBC top to bottom transport east of FC but further north from the M14 section, between the two recirculation cells residing east of FC, is 33.2 ± 3.5 Sv, a value much closer to the M14 observations. Note that this and the following uncertainty values correspond to interannual standard deviation in annual mean transports, rather than variance of 2-day average values as for the (29.8 Sv) model value given previously. It is possible that model details such as bathymetric smoothing may influence the exact position of the model FC recirculations, and hence the apparent DWBC transport one derives without accounting for recirculation. The northward velocity magnitude further east of Flemish Cap in the model is generally higher as well than in the mean M14 section, which is together with the strong southward anomally nearer to FC, is consistent with the idea of a stronger recirculation locally in the model.

Indeed, further upstream, around 53 N, the model (ROMS) top to bottom DWBC transport is 36.5 ± 2.2 Sv, much closer to the M14 (47 N) observations. [14] present and analyze 17-years (1997-2014) of data from an array of moorings maintained across the DWBC at 53 N. They measure the DWBC transport at this latitude at 30.2 ± 6.6 Sv, beneath 400 m depth. This depth approximately corresponds to the upper boundary of LSW at this location. At the same depths the (GB_B) model DWBC transports 26.8 ± 1.8 Sv. Due to water mass bias in our model, the ρ_θ surfaces are considerably less flat than the observations at this depth and location, and hence we calculate the transport under the $\rho_\theta = 27.4$ kg/m^3 surface, which has mean depth close to 400 m in the model at this location. The model result is then 29.3 ± 2.1 Sv, quite close to the observations. Additionally, model velocity within Flemish Pass agrees favorably in pattern (not shown) as well as in total DWBC southward transport (8.4 ± 0.7 Sv) with observations-based estimates ($6.3 - 9.8$ Sv) [15–17]. Note the Flemish Pass transport is substantial relative to the ≈ 30 and ≈ 15 Sv encircling eastern FP, and remaining downstream of FC, respectively (section 3b).

8 Streamfunction calculation by a flood-fill algorithm

Given that large scale flow averaged on isopycnal surfaces is largely geostrophic, it should also be approximately non-divergent. Hence the isopycnal velocity may be used to derive the streamfunction (ψ) locally to a good

approximation [2], by simple integration of the relation

$$d\psi = vdx - udy. \tag{2}$$

To that end, an integration path need be chosen. One simple choice is interleaving integration along lines of constant model coordinate (x and y, approximately zonal or meridional, respectively, in our configuration), where a full line is continuously integrated until the region boundary, followed by integration of the next row in the opposite direction. A disadvantage of the interleaving integration approach is that errors accumulate over very different paths for adjacent pixels in different rows (when interleaving is between rows), hence making the streamfunction less smooth in the interleaving direction. To avoid this pitfall, we adapt a queue (i.e., first-in first-out) flood-fill algorithm [18] to create multiple integration paths, growing outside in a dendritic-like fashion from a chosen initial seed point. A pseudo-algorithm follows. An added advantage is that taking into account "islands" and complex boundaries is accomplished simply by the definition of the mask array (see below).

Derivation of a streamfunction by direct integration of velocity is strictly correct only for a non-divergent velocity distribution. However, the divergent component of the mean flow on potential isopycnal surfaces is relatively small in our results. That is confirmed, by testing that the streamfunction describes the mean circulation to a good approximation (not shown). The mesoscale or larger patterns are confirmed qualitatively by plotting superimposed model velocity fields and the derived approximate ψ. The local velocity field defined by ψ is confirmed on the grid scale by deriving the velocity from $(u_1, v_1) = (-\partial y, \partial x)\psi$, and comparing it with the original (u, v) field. The maximal difference is orders of magnitude smaller than the actual velocity everywhere. That may not be the case using an interleaving integration method, for the velocity component perpendicular to the interleaving direction, as mentioned above. The pseudo-algorithm follows:
0. Initialize a streamfunction array (ψ), and a mask array (M). Set $M = 0$ in masked areas (e.g., land areas, boundary pixels, and other points where the isopycnal surface does not occur), and $M = 1$ elsewhere.
1. Choose an initial grid cell i, which has $M(i) = 1$. Set $\psi(i) = 0$, and $M(i) = 0$. Add pixel i to queue.
2. While queue is not empty,
3. Remove the first pixel (p_1) in queue.
4. For each pixel p which is adjacent to the removed pixel p_1, and for which $M(p) = 1$,
5. Calculate $\psi(p)$ by integrating (2) from p_1 to p. Set $M(p) = 0$.
6. Add pixel p to end of queue.

9 Cluster analysis of the horizontal circulation pattern variability

Here we examine the statistics of the horizontal circulation pattern. We are specifically interested in the typicality of streamline separation from the DWBC, and of the cyclonic recirculations. To achieve this, we perform a cluster analysis of velocity distribution on potential density surfaces. The clustering method used is a single-layer competitive neural network method [19], as implemented in the MATLAB function "competlayer" [20]. The algorithm finds a predefined number N_c of clusters (velocity distributions) that best represent the data in the metric used. Each cluster represents the "best" match to the instantaneous velocity in a Euclidean metric, for a significant number of model time samples.

A qualitative description of the clustering algorithm follows. For a thorough description see [19], and the "competlayer" function description in [20]. Each (2-day mean) GB_B velocity (3-dimensional) output time sample is interpolated onto a chosen (isopycnal) surface S_σ to form a two-dimensional distribution of horizontal velocity, $\underline{V}(t, x_1, x_2)$, which constitutes an input sample for the cluster analysis. The cluster distributions $\underline{V}_n(x_1, x_2)$ are initialized randomly. In the main part of the algorithm, velocity samples $\underline{V}(t, x_1, x_2)$ are randomly drawn from a chosen input set, here all output samples from years 9-16. After each random draw, it is determined which cluster is closest, in a Euclidean metric, to the drawn sample. The closest ("winning") cluster is then adjusted to better represent the sample. At the end of the process, each sample is associated with exactly one cluster. Each cluster is then a velocity distribution which is approximately equally likely in terms of the number of samples closest to it within the input set.

Figure 2 shows results for circulation on $\sigma_1 = 32.43\ kg\ m^{-3}$ using eight clusters. The velocity distribution of each cluster is presented in terms of a streamfunction, for easy comparison with the time-mean circulation pattern. Note that each cluster represents typical circulation conditions during approximately an equal (1/8) fraction of time samples. It is evident that (1) the cyclonic circulations previously identified in the time-mean circulation around FC are present in some form in each of the clusters; (2) the main difference between clusters is the offshore location of the recirculation present east of the southeast FC corner, and (for a smaller fraction of time) its possible coalescence with the recirculation at the northeast corner; (3) the offshore separation of DWBC streamlines occurs in most of the clusters as well (although this is not clear in all panels due to the number of contours used). The clustering is qualitatively insensitive to the prescribed number of clusters (between 4 and

[2] Note the only approximation in (2) is that the full isopycnal velocity is used rather than its rotational component.

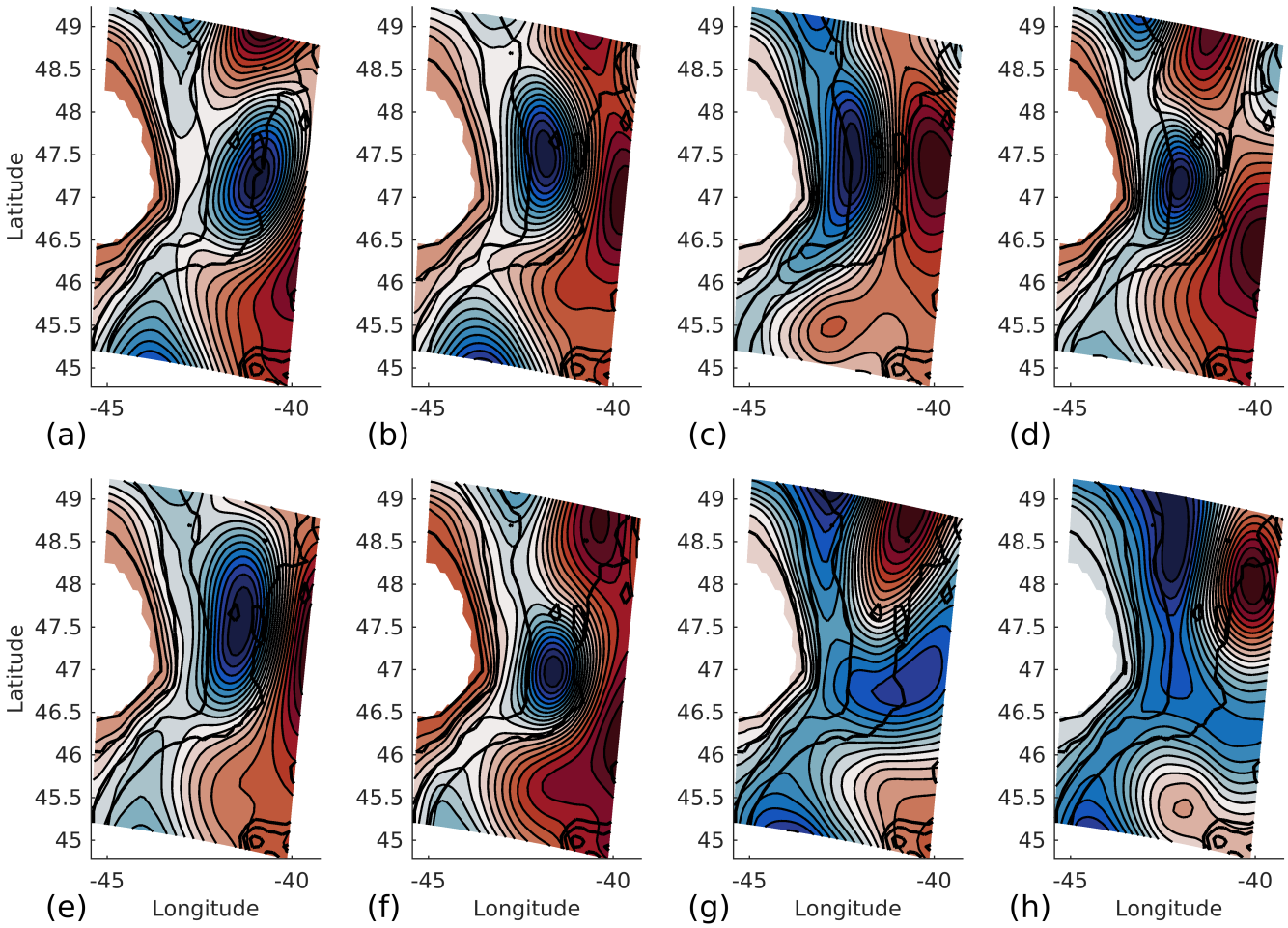

Figure 2: Clustering of the isopycnal circulation around Flemish Cap using a single layer competitive neural network. The clustered variable is velocity along the $\sigma_1 = 32.43\ kg/m^3$ surface between model years 10 and 16. Each panel displays the velocity distribution of a single cluster. Streamfunctions (colors and thin lines) are used rather than, e.g., arrow plots, for effective visualization. The $\{1, 3, 4, 4.5\}\ km$ isobaths are shown in thick black contours. The fraction of time each cluster "occurs" is approximately equal.

36 clusters were attempted, not shown), i.e., essentially no new patterns emerge with an increase in the number of clusters. Rather, clusters look much like combinations of patterns already present in Fig. 2. Therefore, the separation of DWBC streamlines around FC is not just a mean flow pattern (section 3b), but also as a typical flow pattern.

The described results and the main qualitative features identified, are very robust to to changes in the values of the free parameters of the clustering method. Some of the parameter ranges which were tested are: a. choosing up to 36 clusters or as few as 4.; b. variations in the algorithm itself, including using "self-organizing maps" [19]. c. The number of training "epochs". In each epoch each sample is drawn exactly once (and used to calculate and update the winning cluster), in random order. d. Changing the neural network learning rate parameters: Kohonen weight and conscience bias. Trials were conducted with the weights in the ranges $0.001 - 0.05$, and $0.0001 - 0.01$, whereas their default values in "competlayer" are 0.01 and 0.001, respectively. The results are also representative of other mid-depth or deep isopycnal layers as well, including $\sigma_2 = 37.014\ kg/m^3$ which was examined in the time mean (section 3b), as well as depth layers, e.g., $500 - 1000$ or $2000 - 2500\ m$ depth. Enlarging the horizontal area over which the analysis is done also does not change the main results. The clustering area of the results presented in figure 2 was chosen to maximize visibility of the patterns while still capturing most of the area of interest.

References

[1] Patrick Marchesiello, Laurent Debreu, and Xavier Couvelard. Spurious diapycnal mixing in terrain-following coordinate models: The problem and a solution. *Ocean Modelling*, 26(3-4):156–169, 2009.

[2] Florian Lemarié, Jaison Kurian, Alexander F Shchepetkin, M Jeroen Molemaker, François Colas, and James C McWilliams. Are there inescapable issues prohibiting the use of terrain-following coordinates in climate models? *Ocean Modelling*, 42:57–79, 2012.

[3] Lionel Renault, M Jeroen Molemaker, Jonathan Gula, Sebastien Masson, and James C McWilliams. Control and stabilization of the Gulf Stream by oceanic current interaction with the atmosphere. *Journal of Physical Oceanography*, 46(11):3439–3453, 2016.

[4] A. S. Bower, M. S. Lozier, S. F. Gary, and C. W. Böning. Interior pathways of the North Atlantic meridional overturning circulation. *Nature*, 459(7244):243–247, 2009.

[5] Amy Bower, Susan Lozier, and Stefan Gary. Export of Labrador Sea water from the subpolar North Atlantic: a Lagrangian perspective. *Deep Sea Research Part II: Topical Studies in Oceanography*, 58(17-18):1798–1818, 2011.

[6] Claus W Böning. Characteristics of particle dispersion in the North Atlantic: An alternative interpretation of SOFAR float results. *Deep Sea Research Part A. Oceanographic Research Papers*, 35(8):1379–1385, 1988.

[7] Rick Lumpkin, Anne-Marie Treguier, and Kevin Speer. Lagrangian eddy scales in the northern Atlantic Ocean. *Journal of physical oceanography*, 32(9):2425–2440, 2002.

[8] Marie-Isabelle Pujol, Yannice Faugère, Guillaume Taburet, Stéphanie Dupuy, Camille Pelloquin, Michael Ablain, and Nicolas Picot. DUACS DT2014: the new multi-mission altimeter data set reprocessed over 20 years. *Ocean Science*, 12(5), 2016.

[9] Lionel Renault, M Jeroen Molemaker, James C McWilliams, Alexander F Shchepetkin, Florian Lemarié, Dudley Chelton, Serena Illig, and Alex Hall. Modulation of wind work by oceanic current interaction with the atmosphere. *Journal of Physical Oceanography*, 46(6):1685–1704, 2016.

[10] Lionel Renault, Sébastien Masson, Véra Oerder, Swen Jullien, and François Colas. Disentangling the mesoscale ocean-atmosphere interactions. *Journal of Geophysical Research: Oceans*, 124(3):2164–2178, 2019.

[11] Yves Soufflet, Patrick Marchesiello, Florian Lemarié, Julien Jouanno, Xavier Capet, Laurent Debreu, and Rachid Benshila. On effective resolution in ocean models. *Ocean Modelling*, 98:36–50, 2016.

[12] Christian Mertens, Monika Rhein, Maren Walter, Claus W Böning, Erik Behrens, Dagmar Kieke, Reiner Steinfeldt, and Uwe Stöber. Circulation and transports in the Newfoundland Basin, western subpolar North Atlantic. *Journal of Geophysical Research: Oceans*, 119(11):7772–7793, 2014.

[13] Daniel S Wilks. *Statistical methods in the atmospheric sciences*, volume 100. Academic press, 2011.

[14] Rainer Zantopp, Jürgen Fischer, Martin Visbeck, and Johannes Karstensen. From interannual to decadal: 17 years of boundary current transports at the exit of the Labrador Sea. *Journal of Geophysical Research: Oceans*, 122(3):1724–1748, 2017.

[15] P. G. W. Jones J. W. Ramster Hill, H. W. and A. R. Folkard. A note on the Labrador and Atlantic currents to the east of Newfoundland Grand Bank. *ICNAF Res. Doc.*, 116(3082), 1973.

[16] David A Greenberg and Brian D Petrie. The mean barotropic circulation on the Newfoundland shelf and slope. *Journal of Geophysical Research: Oceans*, 93(C12):15541–15550, 1988.

[17] Brian Petrie and Joseph Buckley. Volume and freshwater transport of the labrador current in flemish pass. *Journal of Geophysical Research: Oceans*, 101(C12):28335–28342, 1996.

[18] Theodosios Pavlidis. *Algorithms for graphics and image processing*. Springer Science & Business Media, 2012.

[19] Gérard Dreyfus. *Neural networks: methodology and applications*. Springer Science & Business Media, 2005.

[20] Mark Hudson Beale, Martin T Hagan, and Howard B Demuth. Neural network toolbox user's guide. *The MathWorks Inc*, 2019.